Synergetic Hybrid Aerogels of Vanadia and Graphene as Electrode Materials of Supercapacitors

Xuewei Fu [1], Yuming Chen [2], Yu Zhu [2] and Sadhan C. Jana [1],*

[1] Department of Polymer Engineering, The University of Akron, Akron, OH 44325, USA; xf8@zips.uakron.edu
[2] Department of Polymer Science, The University of Akron, Akron, OH 44325, USA;
   yc67@zips.uakron.edu (Y.C.); yzhu@uakron.edu (Y.Z.)
* Correspondence: janas@uakron.edu; Tel.: +330-972-8293; Fax: +330-972-3406

Abstract: The performance of synergetic hybrid aerogel materials of vanadia and graphene as electrode materials in supercapacitors was evaluated. The hybrid materials were synthesized by two methods. In Method I, premade graphene oxide (GO) hydrogel was first chemically reduced by L-ascorbic acid and then soaked in vanadium triisopropoxide solution to obtain V_2O_5 gel in the pores of the reduced graphene oxide (rGO) hydrogel. The gel was supercritically dried to obtain the hybrid aerogel. In Method II, vanadium triisopropoxide was hydrolyzed from a solution in water with GO particles uniformly dispersed to obtain the hybrid gel. The hybrid aerogel was obtained by supercritical drying of the gel followed by thermal reduction of GO. The electrode materials were prepared by mixing 80 wt % hybrid aerogel with 10 wt % carbon black and 10 wt % polyvinylidene fluoride. The hybrid materials in Method II showed higher capacitance due to better interactions between vanadia and graphene oxide particles and more uniform vanadia particle distribution.

Keywords: supercapacitors; aerogel; hybrid materials; graphene; vanadia

1. Introduction

Supercapacitors have gained considerable attention as energy storage devices due to their high storage capability, excellent discharge-charge rates, long life cycle, and low maintenance costs [1]. Supercapacitors are divided into two categories based on the mechanism of energy storage—(1) electrochemical double-layer capacitors (EDLCs) based on carbon materials, and (2) pseudocapacitors based on electrode materials composed of redox metal oxides or conducting polymers [2]. The capacitance of EDLCs originates from the electrical double-layer formed at the electrode-electrolyte interface. The charge accumulation, in this case, occurs via a non-Faradaic process [2,3]. In the case of pseudocapacitors, the capacitance is derived from a Faradaic process whereby the redox reactions of the electrode materials and the electrolyte occur at the electrode surfaces [4,5].

Graphene aerogels consisting of three-dimensional networks of graphene sheets were considered as electrode materials of supercapacitors in recent investigations [6]. The hierarchically-porous structures with high surface area attributed to aerogels and the high values of electrical conductivity of graphene sheets were found responsible for high specific capacitance of 128 F/g at a current density of 50 mA·g^{-1} [7]. However, higher capacitance than most other EDLCs cannot be achieved due to the limitations imposed by the surface area [2]. Some transition metal oxides with various valences were extensively studied for pseudocapacitance produced via redox reactions of the electrode materials and the electrolyte [2]. Among the transition metal oxides, V_2O_5 is considered a promising electrode material due to its large specific capacitance and easy synthesis process [8]. Although V_2O_5 exhibits satisfactory specific capacitance of 214–346 F/g in KCl [3], its applications and development are

somewhat restricted due to poor cycle stability caused by the collapse of the structures during the charge-discharge process and the low values of electrical conductivity [8–10]. These obstacles must be removed to capitalize on the higher specific capacitance values of V_2O_5, possibly through identification of a set of synergistic materials.

In this work, such a synergy was obtained by combining V_2O_5 and graphene aerogels into single hybrid materials. In these materials, graphene contributes a smooth path for charge transport and provides mechanically stronger structures, while the organized V_2O_5 particles provide a scope for energy storage. This paper presents two facile and green methods for preparation of hybrid aerogels based on V_2O_5 and reduced graphene oxide (rGO). In addition, the synergetic materials in this work avoid the often-encountered compatibility issues of two entirely different materials in the hybrids [11].

2. Experimental

2.1. Materials

Natural graphite powder (99.9995% purity, UCP-1 grade) used in the synthesis of graphene was purchased from Alfa Aesar (Ward Hill, MA, USA). Potassium peroxodisulfate ($\geqslant$99.0%), phosphorus pentoxide ($\geqslant$98.0%), potassium permanganate ($\geqslant$99.9% purity), and acetone ($\geqslant$99.5%) were purchased from Sigma Aldrich (Milwaukee, WI, USA). Hydrogen peroxide (30 wt % solution) was purchased from EMD (Billerica, MA, USA). The precursor material vanadium triisopropoxide (>98.7% purity) and L-ascorbic acid ($\geqslant$99.0% purity) were purchased from VWR Inc. (Radnor, PA, USA). All aqueous solutions and dispersions were produced using deionized (DI) water.

2.2. Preparation of Graphene Oxide Dispersions

Graphite powder was oxidized to graphene oxide (GO) via a modified Hummers method reported elsewhere [6]. Briefly, 12 mL concentrated H_2SO_4 was heated up to 90 °C in a 100 mL beaker. Then 2.5 g $K_2S_2O_8$ and 2.5 g P_2O_5 were added into the beaker with gentle stirring until the materials dissolved completely. The solution was cooled down to 80 °C and 3 g graphite powder was added into it. The mixture was kept at 80 °C for 5 h and then cooled down to room temperature, diluted with 500 mL DI water, and allowed to stand overnight. The solid was filtered, washed with DI water to remove the residual acid, and allowed to dry under ambient conditions. The solid was transferred into 120 mL cold concentrated H_2SO_4 at 0 °C and 15 g $KMnO_4$ was added to it slowly under stirring. The mixture was kept at 35 °C under stirring for 2 h to obtain graphene oxide (GO), after which it was diluted slowly with 250 mL DI water to keep the temperature below 50 °C. The mixture was stirred for 2 h, diluted with 700 mL DI water, and mixed with 20 mL 30 wt % H_2O_2 solution. The mixture containing GO particles was allowed to stand for 12 h and the solid was washed with 1 L 5 wt % HCl solution to remove the metal ions, followed by 1 L DI water to remove the residual acid. GO was dispersed in DI water by ultrasonication for 40 m after which the concentration of GO in the dispersion was adjusted to 7 mg/mL.

2.3. Method I: Preparation of Graphene-Templated Hybrid Aerogel

The hybrid aerogel was prepared in this method using a general procedure reported elsewhere [12]. GO dispersion was diluted to 2 mg/mL and dispersed using ultrasonication for 40 min. L-ascorbic acid (0.42 g) was added into 70 mL GO dispersion under stirring until it completely dissolved. The mixture was heated to 50 °C and allowed to stand for 12 h to form reduced graphene oxide (rGO) gel. The rGO gel was washed with large quantities of DI water over three days to remove the soluble ions and the residual L-ascorbic acid, followed by solvent exchange with acetone for three days to remove water. The graphene gel in acetone was soaked overnight in a solution of 0.8 mL $VO(OC_3H_7)_3$ in 4.5 mL acetone. This allowed diffusion of $VO(OC_3H_7)_3$ molecules into the pores of the graphene gel. The gel was then transferred into another vial filled with 3 mL acetone and 1 mL DI water to induce hydrolysis of $VO(OC_3H_7)_3$ and condensation of vanadium hydroxide into V_2O_5 gel inside the pores of the graphene gel. The molar ratio $VO(OC_3H_7)_3$:water:acetone was kept at 1:60:45. The number of moles (*n*) of $VO(OC_3H_7)_3$ was estimated from the relationship

$n = C_{VO(OC_3H_7)_3} \cdot V_{\text{graphene gel}}$, where $C_{VO(OC3H7)3}$ is the molar concentration of $VO(OC_3H_7)_3$ and $V_{\text{graphene gel}}$ $(=\pi \cdot r^2 \cdot l)$ is the volume of the cylinder of graphene gel, with r and l as the radius and the length of the graphene specimen, respectively.

The hybrid gel was allowed to stand for three days at room temperature for aging, after which the gel was washed with acetone for two days to remove the residual water. The hybrid gel was dried using supercritical CO_2. Three groups of hybrid aerogels were prepared at different concentrations of $VO(OC_3H_7)_3$ with the molar ratio of $VO(OC_3H_7)_3$:H_2O:acetone kept constant. The concentration of $VO(OC_3H_7)_3$ was maintained at 0.64 M, 0.82 M and 1 M, and the corresponding hybrid aerogels are denoted in the rest of the paper as rGO-V_2O_5-0.64, rGO-V_2O_5-0.82, and rGO-V_2O_5-1, respectively.

2.4. Method II: Preparation of Hybrid Aerogel Via One-Pot Synthesis

The hydrolysis of $VO(OC_3H_7)_3$ yields vanadium hydroxide. The polar functional groups, such as –COOH and –OH, on graphene surfaces can interact with vanadium hydroxide or its oligomers. The vanadium hydroxide forms an octahedral complex by one H_2O molecule opposite to the V=O bond, and the hydroxyl group on the graphene oxide surfaces coordinating at the equatorial plane as shown in Figure S1 [13]. These coordination bonds facilitate the growth of VO oligomers and enhance their interactions with the graphene sheets.

A typical preparation process is as follows. 1 mL $VO(OC_3H_7)_3$ and 5 mL acetone were mixed in a vial in an ice bath under vigorous stirring. As gelation of $VO(OC_3H_7)_3$ occurs rapidly, all of the chemicals were kept in an ice bath for 15 min prior to mixing. A 4 mL GO dispersion was added into the vial and mixed to induce hydrolysis of $VO(OC_3H_7)_3$. The concentration of GO in aqueous dispersions was maintained at 2 mg/mL, 4 mg/mL, and 6 mg/mL. The corresponding materials are designated as V_2O_5-rGO-2, V_2O_5-rGO-4, and V_2O_5-rGO-6, respectively, in the rest of the paper.

The resultant liquid was transferred into a cylindrical mold and the gel formed in approximately 1 min. The gel was aged for two days at room temperature in the sealed cylindrical mold. During the aging process, the color of the gel changed from dark red to deep green indicating the presence of V^{4+} ions [14]. The final gel was washed with acetone five times in 5 h intervals to remove the residual water from the gel. The hybrid aerogel was obtained by supercritical drying of the gel using CO_2. The as-prepared aerogel was heated in air at 300 °C for 90 min to reduce GO into graphene [15]. Simultaneously, V^{4+} ions underwent oxidation to V^{5+} ions. In addition, V_2O_5 underwent partial crystallization due to the thermal treatment.

2.5. Characterization

The morphology of the prepared materials was examined by scanning electron microscopy (SEM; JEOL-7401, Boston, MA, USA) and transmission electron microscopy (TEM; JEOL-1230, Boston, MA, USA). X-ray diffraction (Bruker AXS Dimension D8, Billerica, MA, USA) was carried out to study the crystalline structures of the samples. The chemical structures were analyzed by Raman spectroscopy (Horiba LabRam HR, Kyoto, Japan) and Fourier transform infrared spectroscopy (Nicolet 380, Cleveland, OH, USA). The surface properties were characterized by Micromeritics Tristar II 3020 Analyzer (Micromeritics, Norcross, GA, USA), which include Brunauer-Emmett-Teller (BET) surface area and Barrett-Joyner-Halenda (BJH) pore size distribution. The thermal stability of the prepared samples was determined from thermogravimetric analysis (TGA) (TA Instrument, New Castle, DE, USA) in air with a 10 °C/min heating rate and air flow rate of 60 mL/min.

2.6. Electrochemical Measurements

The electrochemical performance of the materials was determined using a symmetrical two-electrode system with 1 M Na_2SO_4 aqueous solution as the electrolyte. The electrode was prepared by mixing 80 wt % hybrid aerogel materials as the active materials, 10 wt % PVDF as the binder, and 10 wt % carbon black as the conducting material into a slurry. The slurry was dropped onto a nickel foam spreading to 1 cm^2 area and the materials were dried at 110 °C for 12 h in vacuum to remove the solvent. The coated nickel foam was then compressed under 10 MPa pressure. The weight of each active material was kept in the range of 0.45–0.5 mg. Cyclic voltammetry (CV) tests with

potential window of −1 to 1 V at scanning rates varying from 10 to 100 mV/s and electrochemical impedance spectroscopy (EIS) with frequency range of 0.01 Hz to 100 kHz were performed on the CHI600E electrochemical workstation (CH Instruments, Inc., Austin, TX, USA). The galvanostatic charge/discharge tests were carried out between −1 to 1 V. The specific capacitance (C) for a single electrode according to the charge/discharge curve was obtained from the following relationship:

$$C = 2I\Delta t/(m\,\Delta V) \tag{1}$$

where I is the applied constant current, m is the mass of the active materials in one electrode, Δt is the discharging time, and ΔV is the potential window.

3. Results and Discussions

3.1. Hybrid Aerogels Produced in Method I

For hybrid aerogels produced in Method I, the concentration of $VO(OC_3H_7)_3$ in solution was varied from 0.64 M to 1 M. The SEM image of rGO aerogel (Figure 1a) shows uniform morphology of randomly-arranged sheet-like structures of graphene. The SEM image of V_2O_5 aerogel presented in Figure 1b displays 3-D networks of rod-like interconnected vanadia particles, which is further verified by the TEM image in Figure 1c. The image in Figure 1c suggests that the building blocks of V_2O_5 aerogel were rod-like structures of typical length approximately 300 nm and diameter several tens of nanometers. Such rod-like structures with typical length 1 μm were reported earlier [16]. The TEM image of the hybrid aerogel rGO-V_2O_5-0.82 in Figure 1d indicates the presence of both rod-like structure of V_2O_5 as in Figure 1c, and the layers of thin sheets of graphene, as seen in Figure 1a. We attribute such a hybrid aerogel structure to the specific gelation process used in Method I.
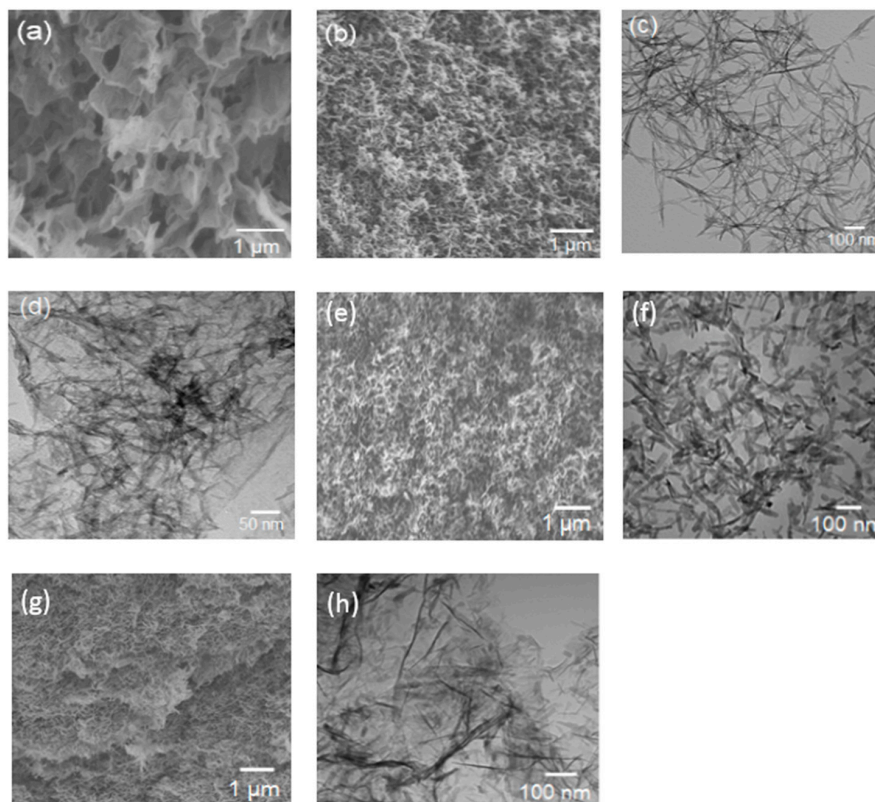
Figure 1. (**a–d**) correspond to Method I: SEM images of (**a**) rGO aerogel and (**b**) V_2O_5 aerogel; TEM images of (**c**) V_2O_5 aerogel and (**d**) rGO-V_2O_5-0.82 hybrid aerogel. (**e–h**) correspond to Method II. (**e**) SEM and (**f**) TEM images of V_2O_5 aerogel; (**g**) SEM image of V_2O_5-rGO-6 hybrid aerogel; and (**h**) TEM image of V_2O_5-rGO-6 hybrid aerogel.

The composition of the as prepared hybrid aerogels was quantitatively determined from the TGA traces generated in air. In Figure S2a, the TGA traces revealed the following trends: gradual weight loss at just above room temperature due to a loss of moisture; weight reduction at close to 200 °C due to the removal of bound water; and the more dramatic weight loss between 300 °C and 350 °C due to the decomposition of the organic groups on graphene [17]. The steep decline in specimen weight at 400–430 °C was due to burning off of graphene [11]. The weight gain after 430 °C is attributed to oxidation of V^{4+} ions to V^{5+} ions. The differences of the residual weights of the hybrid aerogel and that of the V_2O_5 aerogel with the same amount of vanadium isopropoxide in the formulations were used to determine the approximate graphene content in the hybrid aerogels. The graphene contents were found to be 29 wt %, 24 wt %, and 17 wt % respectively for hybrid aerogels rGO-V_2O_5-0.64, rGO-V_2O_5-0.82, and rGO-V_2O_5-1.

The crystal structure of the samples, especially the basal spacing of graphene particles, was inferred from the X-ray diffraction (XRD) patterns as shown in Figure 2. The basal spacing of GO was found to be 0.91 nm which is much larger than that of natural graphite (0.33 nm), indicating that chemical oxidation of graphite to GO was complete in these materials and that the interlayer distance was expanded [18]. In the case of rGO aerogel, the XRD pattern shows a broad peak at around 24°. In addition, the peak at 9.8° corresponding to (001) plane of GO is absent in Figure 2a. This indicates that the method of reduction of GO to graphene using L-ascorbic acid was successful.
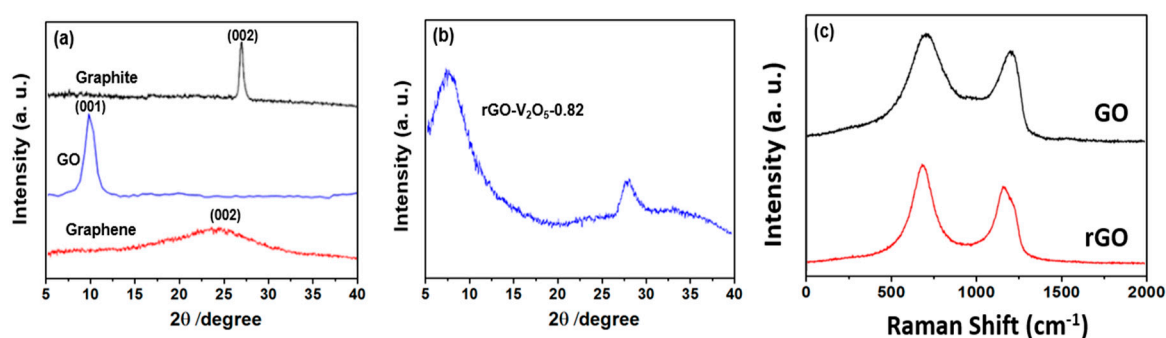
Figure 2. (**a**,**b**) XRD patterns of graphite, GO, graphene, and rGO-V_2O_5-0.82 hybrid aerogel; and (**c**) Raman spectra of GO and rGO.
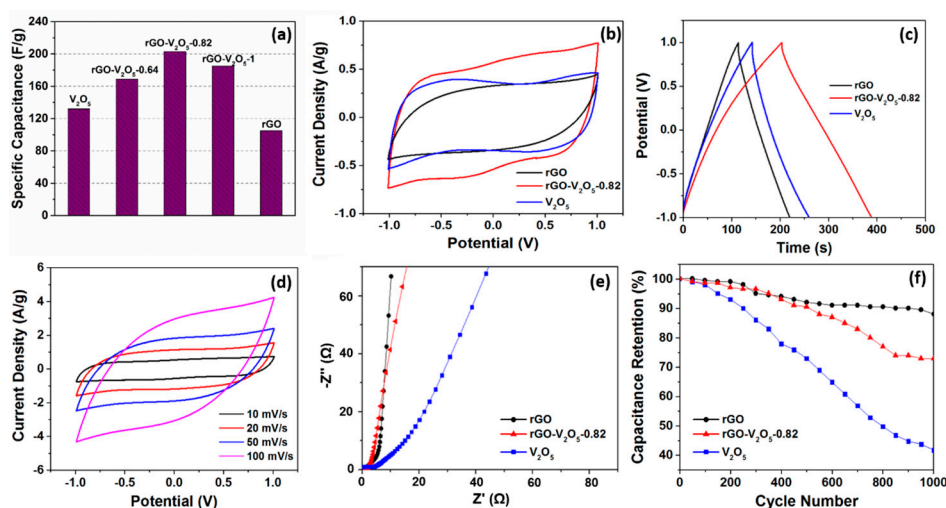
The XRD pattern of the rGO-V_2O_5-0.82 hybrid aerogel revealed only two reflection peaks at around 7.4° and 27.9°, and the low intensity of the peaks suggests a small degree of crystalline order [19]. In view of previous work [20,21], the (001) peak at 7.4° corresponds to the layer stacking of V_2O_5 (d = 1.19 nm) [22,23]. The absence of a graphene peak in the XRD patterns of hybrid aerogels indicates that restacking of graphene sheets did not occur in hybrid aerogels and that graphene was present mostly as single sheets [24]. The FTIR spectra shown in Figure S3 suggests the chemical structures of GO, rGO, and the hybrid aerogels.

Raman spectroscopy was used to determine the quality of graphene by analyzing the intensity ratio of the D- and G-bands. The D-band results from the disorder-induced mode reflecting structural defects and the G-band is associated with the E_{2g} mode from sp^2-hybridized carbon domains [25]. The intensity ratio I_D/I_G reflects the disorder degree of carbon materials [26]. The Raman spectra of GO and rGO aerogel are shown in Figure 2c. There are two obvious peaks at around 1357 cm^{-1} and 1608 cm^{-1} in the Raman spectrum of GO corresponding to the D-band and G-band, respectively. The Raman spectrum of rGO aerogel also shows the D- (at 1343 cm^{-1}) and G-band (at 1585 cm^{-1}). The I_D/I_G ratio of rGO aerogel is 1.24 which is greater than that of GO (1.15) indicating a reduction of the average size of the sp^2 domains [27] when the oxygen groups were removed during the reduction process of GO. In addition, the width of the half-maximum of the G-band was reduced, which suggests a high graphitization degree of rGO aerogel [28].

The presence of platelet-type graphene particles and rod-like vanadia particles in the hybrid aerogels presents several interesting scenarios in terms of solid surface area and pore size distribution. Barrett–Joyner–Halenda (BJH) pore size distributions of rGO aerogel and rGO-V_2O_5-0.82 hybrid aerogel are presented in Figure S4a,b. These were obtained from nitrogen adsorption-desorption isotherms shown in Figure S5. As is evident, the isotherms in Figure S5 are type IV, indicating mesoporous structures. Both samples show mesopores with distinct pore size distribution, as seen in Figure S4. In the case of rGO aerogel, the predominant pores are 4 nm and 60 nm, while those for rGO-V_2O_5-0.82 hybrid aerogel are 4 nm and 40 nm, the latter due to the presence of V_2O_5. The BET specific surface area of rGO-V_2O_5 hybrid aerogels are generally lower than that of rGO aerogel (641 m^2/g), e.g., 396, 348, 299 m^2/g, respectively, for hybrid aerogel specimens rGO-V_2O_5-0.64, rGO-V_2O_5-0.82, and rGO-V_2O_5-1. Note that the specific surface area of V_2O_5 aerogel (254 m^2/g) is much smaller than that of rGO aerogel.

The specific capacitance of the electrodes fabricated using V_2O_5 aerogel, rGO aerogel, and V_2O_5-rGO hybrid aerogels were determined from galvanostatic charge/discharge test data. The values of specific capacitance are shown in Figure 3a. We find that the specific capacitance of the rGO-V_2O_5-0.82 hybrid aerogel calculated from charge/discharge curves are much higher (203 F/g), compared to the rGO aerogel (105 F/g) and the V_2O_5 aerogel (132 F/g). In view of this, the electrochemical performance the rGO-V_2O_5-0.82 hybrid aerogel was further investigated. In Figure 3b, the CV curve of the rGO aerogel exhibits an almost rectangular shape suggesting the EDLC characteristic [3]. In the case of the rGO-V_2O_5-0.82 hybrid aerogel, a pair of redox peaks are observed with a larger area than the V_2O_5 aerogel and the graphene aerogel under the same scanning rate. These indicate that the specific capacitance of the rGO-V_2O_5-0.82 hybrid aerogel is higher than both the rGO and V_2O_5 aerogels along with a Faradaic redox reaction occurring during the charge/discharge process (Figure 3c) [3]. Furthermore, for the hybrid aerogel system, the redox peak is more well-defined, which implies that the presence of graphene improves the utilization of V_2O_5 and, therefore, contributes pseudo-capacitance to the overall capacitance. The CV curves of the rGO-V_2O_5-0.82 hybrid aerogel at varied scan rates (Figure 3d) show a regular and symmetric shape to zero-current line indicating an excellent electrochemical reversibility due to the synergetic effect of EDLC and pseudo-capacitor. The Nyquist plot shown in Figure 3e reveals that rGO aerogel shows an almost ideal EDLC feature with a nearly vertical straight line along the imaginary axis in the low frequency region. Additionally, for the rGO-V_2O_5-0.82 hybrid aerogel, a stronger vertical line than the V_2O_5 aerogel are observed, which is closer to the line for the rGO aerogel. Moreover, the charge transfer resistance (R_{CT}) measured by the diameter of the semicircle in the high-frequency region also reflects the capacitive property [29]. The calculated values of R_{CT} for the rGO aerogel, the V_2O_5 aerogel, and the rGO-V_2O_5-0.82 hybrid aerogel are 0.4 Ω, 3.7 Ω, and 1.7 Ω, respectively. These results indicate that the combination of V_2O_5 and graphene improves the conductivity of the electrode materials and minimizes the ion transportation path.

The cycle stability was tested at 10 A/g of charge/discharge for 1000 cycles (Figure 3f). It can be seen that the degradation of specific capacitance of the rGO aerogel starts from 100 cycles with a consistent, but small, reduction until 1000 cycles exhibiting a characteristic of EDLC. Moreover, the V_2O_5 aerogel shows a quite poor cycle stability due to the structural damage caused by the mechanical stress induced by the ion intercalation-de-intercalation phenomena during the charge-discharge process [30] and dissolution of vanadium oxide [31]. However, the cycle stability of the rGO-V_2O_5-0.82 hybrid aerogel obviously improved, e.g., 73% of initial capacitance. This was achieved due to the presence of graphene nanosheets that were able to withstand the structural changes during the charge-discharge process.

Figure 3. (**a**) Summary of specific capacitance of a series hybrid aerogels prepared by Method I as compared with pure V_2O_5 and rGO aerogels; (**b**) cyclic voltammetry curves of the rGO-V_2O_5-0.82 hybrid aerogel as compared with pure V_2O_5 and rGO aerogels at a scan rate of 10 mV/s; (**c**) galvanostatic charge/discharge curves of rGO and V_2O_5 aerogels and the rGO-V_2O_5-0.82 hybrid aerogel at a current density of 1 A/g; (**d**) CV curves of the rGO-V_2O_5-0.82 hybrid aerogel at a varied scan rate; (**e**) electrochemical impedance spectra measured at a frequency of 0.01 HZ–100 kHZ for the rGO aerogel, the V_2O_5 aerogel, and the rGO-V_2O_5-0.82 hybrid aerogel; and (**f**) cycle stability of the rGO aerogel, the V_2O_5 aerogel, and the rGO-V_2O_5-0.82 hybrid aerogel.

3.2. Hybrid Aerogels from One-Pot Synthesis via Method II

The SEM and TEM images (Figure 1e,f) of the heat-treated V_2O_5 aerogel reveal a randomly-arranged rod-like morphology with lengths less than 100 nm and diameters of several nanometers. These dimensions are much lower than those of the V_2O_5 aerogel and can be attributed to crystallization at the time of thermal treatment. The V_2O_5-rGO-6 hybrid aerogel displays a morphology of crumpled graphene sheets where the growth of V_2O_5 nanofibers is apparent (Figure 1g,h). We note that GO particles were well-dispersed in water and the V_2O_5 nanofibers possibly grew on the surfaces of graphene sheets. The morphology of the V_2O_5-rGO-6 hybrid aerogel further confirms the interaction of VO oligomers with GO sheets in the hydrolysis step.

Figure S2b shows the TGA traces of the samples conducted in air with a heating rate of 10 °C/min. The weight loss of the V_2O_5 aerogel before 150 °C is due to the evaporation of absorbed moisture. In the case of the V_2O_5-rGO hybrid aerogels, there is gradual weight loss from around room temperature to about 400 °C, suggesting that such loss was due to the evaporation of moisture and decomposition of the oxygen-containing groups of GO. In addition, for all hybrid aerogels, a sharp weight reduction occurred in the range of 400 °C to 480 °C, due to the burning of graphene [32]. The graphene weight percent in hybrid aerogels V_2O_5-rGO-2, V_2O_5-rGO-4, and V_2O_5-rGO-6 was estimated to be 12%, 17%, and 23%, respectively.

The X-ray diffraction patterns of the heat-treated V_2O_5 aerogel and V_2O_5-rGO hybrid aerogels (Figure 4a,b) were examined to determine if the heat treatment step used for thermal reduction of GO also caused substantial changes in the crystal structures of the hybrid materials. In Figure 4b, the XRD patterns of a series of V_2O_5-rGO hybrid aerogels exhibit (200), (001), (110), (301), and (310) reflection peaks corresponding to orthorhombic crystalline V_2O_5 (JCPDS No. 41-1426) at the same position as in the case of V_2O_5 aerogel (Figure 4a). These indicate that the V_2O_5-rGO hybrid aerogels were partly crystalline due to the thermal treatment. Additionally, in comparison to V_2O_5 aerogel, no additional peaks are detected in the hybrid aerogels, which indicates high purity of the V_2O_5 parts in the aerogel. The intensity of the XRD reflection peaks shows reduction with an increase of the amount of graphene in the V_2O_5-rGO hybrid aerogels while the peak positions remain the same. This implies that the V_2O_5

layered structure was maintained despite the presence of graphene, although, graphene influenced its crystal formation. The XRD patterns only show V_2O_5 reflection peaks in the V_2O_5-rGO hybrid aerogels, which indicates that V_2O_5 nanofibers prevented restacking of graphene nanosheets [22].
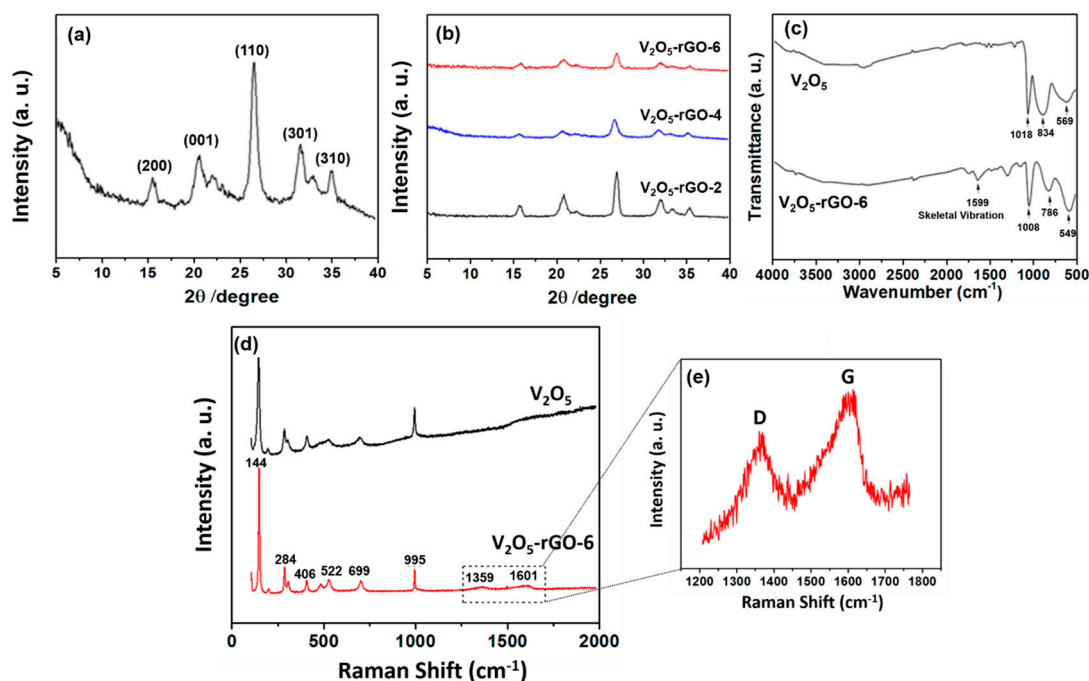
Figure 4. (**a**) XRD patterns of the V_2O_5 aerogel; (**b**) XRD patterns of the V_2O_5-rGO hybrid aerogels with varying weight compositions; (**c**) FTIR spectra of the V_2O_5 and V_2O_5-rGO-6 hybrid aerogels; (**d**,**e**) Raman spectra of the V_2O_5 aerogel and the V_2O_5-rGO-6 hybrid aerogel.

Figure 4c shows FTIR spectra to verify if the thermal reduction method successfully reduced GO to graphene. The characteristic peaks in FTIR spectra at 569, 834, and 1018 cm^{-1} of the V_2O_5 aerogel correspond to triply-coordinated oxygen (chain oxygen) bonds in vanadium oxide, doubly-coordinated oxygen (bridge oxygen) bonds, and stretching vibration of terminal oxygen bonds (V=O), respectively [24]. For V_2O_5-rGO-6 hybrid aerogel, the vanadium oxide characteristic peaks shifted, indicating an interaction of V_2O_5 nanofibers and graphene nanosheets [33]. The bond at 1599 cm^{-1} is observed clearly due to the skeletal vibration of graphene [34].

In Raman spectra shown in Figure 4d,e, the peaks at 144, 284, 406, 522, 699, and 995 cm^{-1} can be observed in both the V_2O_5 aerogel and the V_2O_5-rGO-6 hybrid aerogel, which correspond to the following signatures: skeleton bending vibration of the V-O-V bonds (144 cm^{-1}), bending vibrations of the V=O bonds (284 cm^{-1}), bending vibrations of bridge oxygen bonds (406 cm^{-1}), stretching vibrations of triply-coordinated oxygen bonds (522 cm^{-1}), stretching vibrations of doubly-coordinated oxygen (699 cm^{-1}), and in-phase stretching vibrational of V=O bonds (995 cm^{-1}) [13]. The two peaks at 1359 and 1601 cm^{-1} in the V_2O_5-rGO-6 hybrid aerogel belong to the D- and G-bands of graphene, which suggests a complete reduction of GO and the presence of graphene.

The BJH pore distribution (Figure S4c) of V_2O_5-rGO hybrid aerogels exhibits slightly different distribution from the V_2O_5 aerogel, especially the V_2O_5-rGO-6 hybrid aerogel shows a peak at 40 nm. This pore size distribution of the two types of samples might have some effect on the electrochemical property because the mesopores provide more accessibility for ion transportation [35]. The BET-specific surface areas of the samples are listed in Tables 1 and 2.

The BET-specific surface area of the V_2O_5-rGO-6 hybrid aerogel (392 cm^2/g) is much larger than the V_2O_5 aerogel (213 cm^2/g), which resulted from the presence of high surface area graphene nanosheets. This has the potential to provide much higher capacity for energy storage. Note in this case that the surface area of V_2O_5 aerogel listed in Table 2 is lower than that reported in Table 1. After annealing, the pore structure of the V_2O_5 aerogel changed due to the oxidation of VO_x and

partial crystallization of V_2O_5. Thus, the BET-specific surface area of the heat-treated V_2O_5 aerogel reduced to 213 $m^2 \cdot g^{-1}$. For a supercapacitor, especially for hybrid electrodes, the surface area serves as a significant factor for charge storage that provides space for Faradaic redox reactions to produce pseudocapacitance. In this way, the large specific surface area of the V_2O_5-rGO hybrid aerogel favors capacitance.

Table 1. BET-specific surface area of the V_2O_5, graphene, and V_2O_5-rGO hybrid aerogels prepared by Method I.

Sample	V_2O_5	Graphene	V_2O_5-rGO-0.64	V_2O_5-rGO-0.82	V_2O_5-rGO-1
SSA/$m^2 \cdot g^{-1}$	254	641	396	348	299

Table 2. BET-specific surface area of the V_2O_5 aerogel and V_2O_5-rGO hybrid aerogels prepared by Method II.

Sample	V_2O_5	V_2O_5-rGO-2	V_2O_5-rGO-4	V_2O_5-rGO-6
SSA/$m^2 \cdot g^{-1}$	213	282	357	392

The specific capacitance was obtained from the data of charge-discharge curves and calculated from Equation (1). The galvanostatic charge/discharge curves of the different V_2O_5-rGO hybrid aerogels are shown in Figure 5a. It can be seen that the specific capacitance of the V_2O_5-rGO hybrid aerogel is generally higher than the V_2O_5 aerogel (98 F/g). In addition, an increase in specific capacitance is observed for materials with higher content of graphene in the V_2O_5-rGO hybrid aerogels. The specific capacitance of a series of V_2O_5-rGO hybrid aerogels, respectively, for the V_2O_5-rGO-2, V_2O_5-rGO-4, and V_2O_5-rGO-6 hybrid aerogels are 163, 202, and 272 F/g, which are summarized in Figure 5b. This tendency is led by a synergetic effect of V_2O_5 and graphene, in which graphene enhances the conductivity and increases the specific surface area of the V_2O_5-rGO hybrid aerogels in order to promote better utilization of V_2O_5.
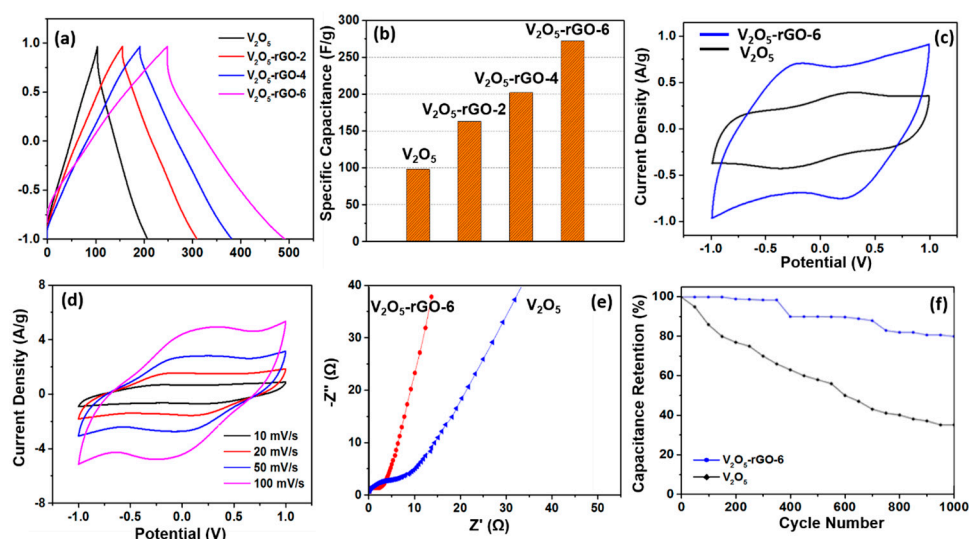
Figure 5. (**a**) Galvanostatic charge/discharge curves of the V_2O_5 and V_2O_5-rGO hybrid aerogels with different ratios at a current density of 1 A/g; (**b**) summary of specific capacitance of the V_2O_5 and V_2O_5-rGO hybrid aerogels; (**c**) CV curves of the V_2O_5 and V_2O_5-rGO-6 hybrid aerogel at a scan rate of 10 mV/s; (**d**) CV curves of the V_2O_5-rGO-6 hybrid aerogel at varying scan rates; (**e**) EIS of the V_2O_5 and V_2O_5-rGO-6 hybrid aerogel measured at a frequency of 0.01 HZ–100 kHZ; and (**f**) cycle stability of the V_2O_5 and V_2O_5-rGO-6 hybrid aerogels tested at a current density of 10 A/g.

Since the specific capacitance of the V_2O_5-rGO-6 hybrid aerogel is the highest among the three materials studied, further investigation of its electrochemical performance was conducted. The cyclic voltammetry curves of both samples are shown in Figure 5c. The shape of CV curves of both materials is symmetrical, suggesting an electrochemical reversibility. These curves deviated from an ideal rectangle indicating the Faradic pseudocapacitance. A pair of redox peaks of potentials at around 0.32 V and 0.30 V resulted from the transformation between V^{5+} and V^{4+}. However, the CV curve of the V_2O_5-rGO-6 hybrid aerogel shows undefined redox peaks, which are possibly caused by the EDLC contribution by graphene. This result further confirms the synergetic effect of the double-layer capacitance and pseudocapacitance [36]. The area of the CV curve of the V_2O_5-rGO-6 hybrid aerogel is much larger than that of the V_2O_5 aerogel, and this also confirms a higher specific capacitance of the V_2O_5-rGO-6 hybrid aerogel. The CV curves of the V_2O_5-rGO-6 hybrid aerogel at different scan rates are shown in Figure 5d in order to further study the capacitive performance. As the scan rate increases, the quasi-rectangular shape of the CV curves is affected, although the shape of the curves remains mirror-symmetric with zero-current line even at the high scan rate of 100 mV/s. This result implies a high rate performance and good capacitive reversibility [37]. Note that the specific capacitance of the V_2O_5-rGO-6 hybrid aerogel is much higher than that of graphene-templated rGO-V_2O_5-0.82 hybrid aerogel (203 F·g^{-1}) produced in Method I with a similar amount of graphene, even if V_2O_5 is partly crystalline due to the thermal reduction for the V_2O_5-rGO-6 hybrid aerogel.

It can be concluded from the data presented up to this point that the preparation method strongly influenced the structure-properties relationships and the final electrochemical performance. In Method I, the capillary force contributed to selective localization of V_2O_5 on the graphene nanosheets. Additionally, the unavoidable diffusion gradient quite possibly led to a heterogeneous dispersion of V_2O_5 within the rGO aerogel produced by Method I. In Method II, the recombination of V_2O_5 and graphene in hybrid aerogels was easily accomplished and enhanced by the coordination bonds between V_2O_5 and graphene nanosheets that are much stronger than the capillary force in Method I. Meanwhile, the uniform mixing of V_2O_5 and graphene also produces a homogeneous hybrid structure in Method II. In addition, the BET-specific surface area of the V_2O_5-rGO-6 hybrid aerogel is greater than the rGO-V_2O_5-0.82 hybrid aerogel, suggesting that there is more capacity for energy storage in hybrid materials produced by Method II. These factors answer why the hybrid aerogels from Method I exhibit inferior electrochemical performance than hybrid aerogels produced by Method II.

The Nyquist plots of EIS of V_2O_5 aerogel are shown in Figure 5e. The corresponding equivalent circuit is presented in Figure S6. In comparison, the V_2O_5-rGO-6 hybrid aerogel has more vertical lines parallel to the imaginary axis than the V_2O_5 aerogel, which indicates that the electrical conductivity of the hybrid aerogel was improved or the accessibility of ions in the electrolyte was enhanced due to the combination of the structures from graphene and V_2O_5 and, therefore, exhibited a behavior more closely to that of an ideal supercapacitor. The cycle stabilities of the V_2O_5 aerogel and the V_2O_5-rGO-6 hybrid aerogel were characterized by a charge/discharge test over 1000 cycles at a constant current density of 10 A/g shown in Figure 5f. This indicates clearly that the capacitance retention of the V_2O_5-rGO-6 hybrid aerogel was 80% after 1000 operation cycles, while the capacitance retention of the V_2O_5 aerogel was only 35% of the initial specific capacitance. The low capacitance retention of the V_2O_5 aerogel can be attributed to the structural damage caused by the insertion and desertion of electrolyte ions during the charge/discharge process [38] and two clear drops after 350th and 700th cycles could be possibly caused by the large structural changes of V_2O_5. According to published literature, pure V_2O_5 shows very poor cycle stability up to only 100 cycles in aqueous electrolyte [19]. Obviously, the addition of graphene improved the cycle stability for the materials developed in this work due to its electroactive property.

4. Conclusions

This study considered two methods for the preparation of hybrid aerogels of V_2O_5 and rGO. The specific capacitance of hybrid materials prepared by Method I increased to 202 F/g with 23 wt % graphene. Such improved capacitance is due to the synergy derived from the higher electrical conductivity of graphene, the greater contact between the electrode and electrolyte due to higher

surface area, and the pseudocapacitance of V_2O_5. The hybrid materials prepared by one-pot synthesis route in Method II produced much higher capacitance of 272 F/g at 23 wt % graphene content and exhibited improved cycle stability due to better interaction of V_2O_5 particles with graphene surfaces and homogeneous dispersion of the precursor materials.

Supplementary Materials: Supplementary materials can be found at http://www.mdpi.com/2311-5629/2/3/21/s1.

Author Contributions: Xuewei Fu and Sadhan C. Jana conceived and designed the experiments; Xuewei Fu and Yuming Chen performed the experiments; Xuewei Fu and Yuming Chen analyzed the data; Xuewei Fu wrote the first draft; Sadhan C. Jana and Yu Zhu modified the draft. All authors reviewed the final draft.

Conflicts of Interest: The authors declare no conflict of interest.

References

1. Kötz, R.; Carlen, M. Principles and Applications of Electrochemical Capacitors. *Electrochim. Acta* **2000**, *45*, 2483–2498. [CrossRef]

2. Zhi, M.; Xiang, C.; Li, J.; Li, M.; Wu, N. Nanostructured Carbon–Metal Oxide Composite Electrodes for Supercapacitors: A Review. *Nanoscale* **2013**, *5*, 72–88. [CrossRef] [PubMed]

3. Fu, M.; Ge, C.; Hou, Z.; Cao, J.; He, B.; Zeng, F.; Kuang, Y. Graphene/vanadium Oxide Nanotubes Composite as Electrode Material for Electrochemical Capacitors. *Physica B* **2013**, *421*, 77–82. [CrossRef]

4. Jiang, H.; Ma, J.; Li, C. Mesoporous Carbon Incorporated Metal Oxide Nanomaterials as Supercapacitor Electrodes. *Adv. Mater.* **2012**, *24*, 4197–4202. [CrossRef] [PubMed]

5. Lokhande, C.D.; Dubal, D.P.; Joo, O.S. Metal Oxide Thin Film Based Supercapacitors. *Curr. Appl. Phys.* **2011**, *11*, 255–270. [CrossRef]

6. Zeng, F.; Feng, G.; Nguyen, S.T.; Duong, H.M. Advanced Multifunctional Graphene Aerogel–Poly (methyl methacrylate) Composites: Experiments and Modeling. *Carbon* **2015**, *81*, 396–404.

7. Zhang, X.; Sui, Z.; Xu, B.; Yue, S.; Luo, Y.; Zhan, W.; Liu, B. Mechanically Strong and Highly Conductive Graphene Aerogel and Its Use as Electrodes for Electrochemical Power Sources. *J. Mater. Chem.* **2011**, *21*, 6494–6497. [CrossRef]

8. Choi, D.; Blomgren, G.E.; Kumta, P.N. Fast and Reversible Surface Redox Reaction in Nanocrystalline Vanadium Nitride Supercapacitors. *Adv. Mater.* **2006**, *18*, 1178–1182. [CrossRef]

9. Niu, Z.; Liu, L.; Zhang, L.; Shao, Q.; Zhou, W.; Chen, X.; Xie, S. A Universal Strategy to Prepare Functional Porous Graphene Hybrid Architectures. *Adv. Mater.* **2014**, *26*, 3681–3687. [CrossRef] [PubMed]

10. Wang, X.; Jana, S.C. Synergistic Hybrid Organic–Inorganic Aerogels. *ACS Appl. Mater. Interfaces* **2013**, *5*, 6423–6429. [CrossRef] [PubMed]

11. Sathiya, M.; Prakash, A.S.; Ramesha, K.; Tarascon, J.M.; Shukla, A.K. V_2O_5-Anchored Carbon Nanotubes for Enhanced Electrochemical Energy Storage. *J. Am. Chem. Soc.* **2011**, *133*, 16291–16299. [CrossRef] [PubMed]

12. Livage, J. Sol-gel Chemistry and Electrochemical Properties of Vanadium Oxide Gels. *Solid State Ionics* **1996**, *86*, 935–942. [CrossRef]

13. Wang, Z.; Xu, D.; Huang, Y.; Wu, Z.; Wang, L.; Zhang, X. Facile, Mild and Fast Thermal-decomposition Reduction of Graphene Oxide in Air and Its Application in High-Performance Lithium Batteries. *Chem. Commun.* **2012**, *48*, 976. [CrossRef] [PubMed]

14. Augustyn, V.; Dunn, B. Low-potential Lithium-ion Reactivity of Vanadium Oxide Aerogels. *Electrochim. Acta.* **2013**, *88*, 530–535. [CrossRef]

15. Chaput, F.; Dunn, B.; Fuqua, P.; Salloux, K. Synthesis and Characterization of Vanadium Oxide Aerogels. *J. Non Crystalline Solids* **1995**, *188*, 11–18. [CrossRef]

16. Wang, G.; Yang, J.; Park, J.; Gou, X.; Wang, B.; Liu, H.; Yao, J. Facile Synthesis and Characterization of Graphene Nanosheets. *J. Phys. Chem. C* **2008**, *112*, 8192–8195. [CrossRef]

17. Le, D.B.; Passerini, S.; Guo, J.; Ressler, J.; Owens, B.B.; Smyrl, W.H. High Surface Area V_2O_5 Aerogel Intercalation Electrodes. *J. Electrochem. Soc.* **1996**, *143*, 2099–2104. [CrossRef]

18. Petkov, V.; Trikalitis, P.N.; Bozin, E.S.; Billinge, S.J.L.; Vogt, T.; Kanatzidis, M.G. Structure of $V_2O_5 \cdot nH_2O$ Xerogel Solved by the Atomic Pair Distribution Function Technique. *J. Am. Chem. Soc.* **2002**, *124*, 10157–10162. [CrossRef] [PubMed]

19. Yu, J.; Liu, S.; Cheng, B.; Xiong, J.; Yu, Y.; Wang, J. Polymer-directed Large-scale Synthesis of Single-Crystal Vanadium Oxide Nanobelts. *Mater. Chem. Phys.* **2006**, *95*, 206–210. [CrossRef]

20. Baddour, R.; Pereira-Ramos, J.P.; Messina, R.; Perichon, J. A Thermodynamic, Structural and Kinetic Study of the Electrochemical Lithium Intercalation into the Xerogel $V_2O_5 \cdot 1.6\ H_2O$ in a Propylene. *J. Electroanal. Chem.* **1991**, *314*, 81–101. [CrossRef]

21. Aldebert, P.; Baffier, N.; Gharbi, N.; Livage, J. Intercalation de Solvants Organiques Polaires dans la Structure Lamellaire des gels de V_2O_5. *Mater. Res. Bull.* **1981**, *16*, 669–676. [CrossRef]

22. He, H.; Gao, C. Supraparamagnetic, Conductive, and Processable Multifunctional Graphene Nanosheets Coated with High-Density Fe_3O_4 Nanoparticles. *ACS Appl. Mater. Interfaces* **2010**, *2*, 3201–3210. [CrossRef] [PubMed]

23. Jeong, H.K.; Jin, M.H.; An, K.H.; Lee, Y.H. Structural Stability and Variable Dielectric Constant in Poly Sodium 4-Styrensulfonate Intercalated Graphite Oxide. *J. Phys. Chem. C* **2009**, *113*, 13060–13064. [CrossRef]

24. Zhou, X.; Wu, G.; Wu, J.; Yang, H.; Wang, J.; Gao, G.; Cai, R.; Yan, Q. Multiwalled Carbon Nanotubes–V_2O_5 Integrated Composite with Nanosized Architecture as a Cathode Material for High Performance Lithium Ion Batteries. *J. Mater. Chem. A* **2013**, *1*, 15459–15468. [CrossRef]

25. Park, S.H.; Bak, S.M.; Kim, K.H.; Jegal, J.P.; Lee, S.I.; Lee, J.; Kim, K.B. Solid-state Microwave Irradiation Synthesis of High Quality Graphene Nanosheets under Hydrogen Containing Atmosphere. *J Mater. Chem* **2011**, *21*, 680–686. [CrossRef]

26. Wu, Z.S.; Ren, W.; Gao, L.; Zhao, J.; Chen, Z.; Liu, B.; Tang, D.; Yu, B.; Jiang, C.; Cheng, H.M. Synthesis of Graphene Sheets with High Electrical Conductivity and Good Thermal Stability by Hydrogen Arc Discharge Exfoliation. *ACS Nano.* **2009**, *3*, 411–417. [CrossRef] [PubMed]

27. Tuinstra, F.; Koenig, J.L. Raman Spectrum of Graphite. *J Chem. Phys.* **1970**, *53*, 1126–1130. [CrossRef]

28. Ferrari, A.C.; Robertson, J. Raman Spectroscopy of Amorphous, Nanostructured, Diamond–Like Carbon, and Nanodiamond. *R. Soc. A: Math. Phys. Eng. Sci.* **2004**, *362*, 2477–2512. [CrossRef] [PubMed]

29. Yang, S.B.; Feng, X.L.; Ivanovici, S.; Müllen, K. Fabrication of Graphene-Encapsulated Oxide Nanoparticles: Towards High-Performance Anode Materials for Lithium Storage. *Angew. Chem. Int. Ed.* **2010**, *49*, 8408–8411. [CrossRef] [PubMed]

30. Reddy, R.N.; Reddy, R.G. Porous Structured Vanadium Oxide Electrode Material for Electrochemical Capacitors. *J. Power Sources* **2006**, *156*, 700–704. [CrossRef]

31. Liu, Y.; Clark, M.; Zhang, Q.; Yu, D.; Liu, D.; Liu, J.; Cao, G. V_2O_5 Nano-Electrodes with High Power and Energy Densities for Thin Film Li-Ion Batteries. *Adv. Energy Mater.* **2011**, *1*, 194–202. [CrossRef]

32. Du, G.; Seng, K.H.; Guo, Z.; Liu, J.; Li, W.; Jia, D.; Cook, C.; Liu, Z.; Liu, H. Graphene–$V_2O_5 \cdot nH_2O$ Xerogel Composite Cathodes for Lithium Ion Batteries. *RSC Adv.* **2011**, *1*, 690–697. [CrossRef]

33. Wang, H.W.; Yi, H.; Chen, X.; Wang, X.F. One-step Strategy to Three-Dimensional Graphene/VO_2 Nanobelt Composite Hydrogels for High Performance Supercapacitors. *J. Mater. Chem. A* **2014**, *2*, 1165–1173. [CrossRef]

34. Wang, J.L.; Shi, Z.X.; Fan, J.C.; Ge, Y.; Yin, J.; Hu, G.X. Self-assembly of Graphene into Three-Dimensional Structures Promoted by Natural Phenolic Acids J. *Mater. Chem.* **2012**, *22*, 22459–22466. [CrossRef]

35. Wei, T.Y.; Chen, C.H.; Chien, H.C.; Lu, S.Y.; Hu, C.C. A Cost-Effective Supercapacitor Material of Ultrahigh Specific Capacitances: Spinel Nickel Cobaltite Aerogels from an Epoxide-Driven Sol–Gel Process. *Adv. Mater.* **2010**, *22*, 347–351. [CrossRef] [PubMed]

36. Zhang, J.T.; Jiang, J.W.; Li, H.L.; hao, X.S. A High-Performance Asymmetric Supercapacitor Fabricated with Graphene-Based Electrodes. *Energy Environ. Sci.* **2011**, *4*, 4009–4015. [CrossRef]

37. Boukhalfa, S.; Evanoff, K.; Yushin, G. Atomic Layer Deposition of Vanadium Oxide on Carbon Nanotubes for High-Power Supercapacitor Electrodes. *Energy Environ. Sci.* **2012**, *5*, 6872–6879. [CrossRef]

38. Toupin, M.; Brousse, T.; Belanger, D. Influence of Microstucture on the Charge Storage Properties of Chemically Synthesized Manganese Dioxide. *Chem. Mater.* **2002**, *14*, 3946–3952. [CrossRef]